Reviews on Advanced Materials and Technologies, 2024, vol. 6, no. 2, pp. 47–61
DOI: 10.17586/2687-0568-2024-6-2-47-61

Computational Analysis of SiC Crystal Growth from Silicon Melt Diluted with Cr, Fe, Co, Ni, Y, Al, La, Ce, Pr, Nd, and Sc. Part 1

Andrei N. Vorob'ev[1,2,*]

[1] STR Group, Inc. – Soft-Impact, Ltd., Office 603, Bol'shoy Sampsonievskiy pr., 64, lit. E, St. Petersburg, 194044, Russia
[2] Sci-Tech Center "Glass and Ceramics", Ltd., Dudko 3, St. Petersburg, 192029, Russia

Article history

Received April 03, 2024
Received in revised form, May 13, 2024
Accepted May 22, 2024
Available online June 30, 2024

Abstract

The effect of various co-solvents on silicon carbide growth from solutions is sequentially analyzed within computational approach. The information related to the problem is collected from available literature and thoroughly treated. Boundary between liquid and solid state of solutions (liquidus line) is found from phase diagrams of 11 binary systems and is accounted for in calculating the carbon solubility at temperature and composition varying in a wide range. Thermophysical and transport properties are collected for preliminary estimation and comparison of growth rates. Their saturation with co-solvent percentage is predicted. Two-dimensional problem is set and first computations are demonstrated. It is shown that addition of lanthanum to the silicon melt gives a significantly higher growth rate than that of chromium.

Keywords: SiC growth; Silicon melt; Solution; Carbon solubility; CGSim (crystal growth simulation)

1. INTRODUCTION

The superior physical properties of silicon carbide (SiC) provide an equivalent replacement of silicon for high power and high-temperature electronics. These advantages allow us to hope that the industry could completely replace silicon in devices by SiC in the future. SiC technologies have made tremendous strides in last years, with a variety of encouraging device and circuit demonstrations.

Some effective techniques for producing the SiC crystal of high quality have been developed. Among them, SiC top-seeded solution growth (TSSG) method turns out to be a worthy opponent to such methods as the physical vapor transport (PVT) and the high temperature vapor deposition (HTCVD). However, when using the pure silicon melt, only a low growth rate can be achieved due to low carbon solubility. To enhance it, several co-solvents are added recently. Comprehensive review of the topic is presented in Ref. [1]. Let us emphasize main features here. Solution growth is a standard technology for preparing compound semiconductors [2]. For solution growth of SiC single crystal by TSSG, the Si source stems from highly pure Si melt while the graphite crucible serves dual purposes: heater and C solute source. SiC single crystals are more likely to grow under the ideal stoichiometric ratio when the ratio of C and Si is close to 1, indicating a lower defect density [3]. The driving force of the growth is the C supersaturation that is dominated by temperature gradient and solution system. There is a generally accepted viewpoint that the higher the C supersaturation, the faster the growth rate, while low C supersaturation produces a smooth surface [4]. Doping transition metal elements or rare-earth elements not only effectively lower the growth temperature but seems to be the only way to drastically improve carbon solubility in Si melt [1]. To date, 4-inch SiC substrates with a thickness of 15 mm have been grown by TSSG method, while substrates of 6 inches and larger are still in progress. Multi-parameters of the solution growth including meniscus, solvent design, flow control etc. make high-quality single crystal growth possible.

* Corresponding author: Andrei N. Vorob'ev, e-mail: andrei.vorobiev@str-soft.com

Note that the appearance of defects, the unintentional doping of crystals by fluxes and other parameters of as-grown crystals are shelved within the present paper. To investigate them properly, a specific tool should be used. The present paper sets a more limited problem to reveal and to compare the effect of such co-solvents as Cr, Fe, Co, Ni, Y, Al, La, Ce, Pr, Nd and Sc only on numerical values of the carbon solubility and the SiC growth rate depending on process conditions. Uniformity of the growth rate distribution on the seed surface is planned to analyze within 2D approach for estimating the morphology in further parts of the paper. To solve the limited problem, the thermodynamics of non-ideal solutions is applied for calculating the carbon solubility and the SiC growth rate is evaluated from the carbon flux onto the seed. In addition, the author does not aim here to reproduce all available experiments due to the fact that none of models can do it. Nevertheless, the collation of various liquid alloys within a reasonable approach can help one to catch main trends and features of the considered technology.

2. PRELIMINARY ANALYSIS

2.1. Liquidus lines of binary system Si-Me, Me = Cr, Fe, Co, Ni, Y, Al, La, Ce, Pr, Nd and Sc

Silicon melt is known to be a source of Si-atoms involved in SiC TSSG and acts as a basic solvent with melting point of 1685 K [1]. Obviously, the process using the pure silicon should be run at temperatures higher than this threshold value. The temperature limitations for solutions additionally depend on co-solvent percentage and are represented as phase diagrams calculated from measurements and separating the liquid and solid states. Therefore, before any analysis it is useful to get exhaustive information on when the silicon diluted with one of co-solvents or their composition remains liquid.

Solid-liquid phase diagrams of binary solutions listed above were found in available literature [5–15] and treated. As a result, the corresponding liquidus lines were plotted in Fig. 1 to compare them against each other and to clear up the applicability of one or another solution. As seen from the plots, the threshold temperatures vary nonmonotonically and differently with mole fraction of considered co-solvents or fluxes. Melting point of all solutions with doping up to 20–30 mol.% becomes lower than that of the pure silicon. After that, with the exception of Si-Al (solid blue) and Si-Ni (long dashed red), liquidus temperatures sharply rise especially in the case of lanthanides, Y and Sc. It means that the temperature should be elevated significantly for keeping the solution in liquid state at the co-solvent fraction varying from 30 to 70 mol.%

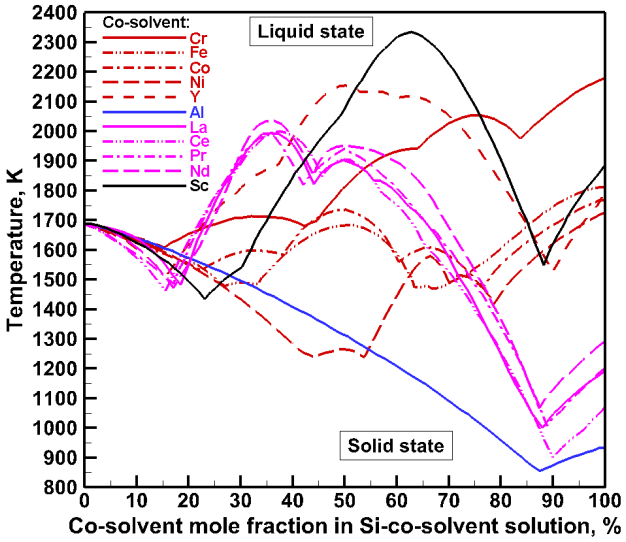

Fig. 1. Liquidus-solidus of Si-Me alloys, where Me = Cr, Fe, Co, Ni, Y, Al, La, Ce, Pr, Nd, Sc. Regions of liquid phase are located higher than liquidus curves.

Note that being close to each other, Si-lanthanide liquidus curves (purple) reach a maximum somewhat lower than 2100 K at ≈ 35 mol.% and decrease to 900–1100 K at ≈ 90 mol.%. Most severe temperatures of 2100–2400 K are observed for Si-Y (dashed red) and Si-Sc (solid black) at 50% Y and 60% Sc, respectively, going down to 1600 K at ≈ 90 mol.%.

Si-Cr liquidus (solid red) increases between melting points of solvents with weekly pronounced local maximums and minimums. Ni-doping provides the threshold of 1300 K at 40–55% Ni. Si-Fe (dashed dot dot red) and Si-Co (dashed dot red) systems show similar dependences without some apparent features.

Unlike others, only Si-Al system exhibits the classical behavior with the single eutectics at ≈ 87% Al.

The information above is collected in Table 1 and can be used for a preliminary selection of co-solvents, providing the liquid binary solutions. Moreover, the temperature limitations are further accounted for in calculating the carbon solubility and the SiC growth rate.

2.2. Thermodynamic background

For describing the SiC crystal growth from multi-component solutions, one should formulate the boundary conditions containing the carbon solubility. To evaluate it at temperature and solvents composition varying in a wide range, the well-known relations of thermodynamics are applied [16]. Assuming that the SiC crystal dipped into Si-Me solution partly dissolves producing the carbon through the chemical reaction

$$Si_{(liquid)} + C_{(dissolved)} \rightleftarrows SiC_{(solid)}, \quad (1)$$

Table 1. Lists of liquid binary alloys vs temperature and composition.

Mole fraction of co-solvent added to silicon melt	Temperature, K					
	1700–1800	1800–1900	1900–2000	2000–2100	2100–2200	2200–2300
0.1–0.2	All co-solvents	All co-solvents	All co-solvents	All co-solvents	All co-solvents	All co-solvents
0.2–0.3	Fe, Co, Ni, Al, Sc	All co-solvents	All co-solvents	All co-solvents	All co-solvents	All co-solvents
0.3–0.4	Fe, Co, Ni, Al	Fe, Co, Ni, Al, Cr	Fe, Co, Ni, Al, Cr, Sc	Fe, Co, Ni, Al, Cr, Sc, Y, La, Ce, Pr	All co-solvents	All co-solvents
0.4–0.5	Fe, Ni, Al	Fe, Ni, Al, Co	Fe, Ni, Al, Co, Cr	Fe, Ni, Al, Co, Cr, La, Ce, Pr, Nd	Fe, Ni, Al, Co, Cr, La, Ce, Pr, Nd, Sc	All co-solvents
0.5–0.6	Fe, Ni, Al	Fe, Ni, Al, Co	Fe, Ni, Al, Co, La, Ce	Fe, Ni, Al, Co, La, Ce, Pr, Nd, Cr	Fe, Ni, Al, Co, La, Ce, Pr, Nd, Cr	Fe, Ni, Al, Co, La, Ce, Pr, Nd, Cr, Y
0.6–0.7	Fe, Co, Ni, Al	Fe, Co, Ni, Al, La, Ce	Fe, Co, Ni, Al, La, Ce, Pr, Nd	Fe, Co, Ni, Al, La, Ce, Pr, Nd	Fe, Co, Ni, Al, La, Ce, Pr, Nd, Cr	Fe, Co, Ni, Al, La, Ce, Pr, Nd, Cr, Y
0.7–0.8	Fe, Co, Ni, Al, La, Ce, Pr, Nd	Fe, Co, Ni, Al, La, Ce, Pr, Nd	Fe, Co, Ni, Al, La, Ce, Pr, Nd	Fe, Co, Ni, Al, La, Ce, Pr, Nd	Fe, Co, Ni, Al, La, Ce, Pr, Nd, Cr, Y	Fe, Co, Ni, Al, La, Ce, Pr, Nd, Cr, Y
0.8–0.9	Co, Ni, Al, La, Ce, Pr, Nd	Co, Ni, Al, La, Ce, Pr, Nd, Fe	Co, Ni, Al, La, Ce, Pr, Nd, Fe, Y, Sc	Co, Ni, Al, La, Ce, Pr, Nd, Fe, Y, Sc	All co-solvents	All co-solvents

one can write the following equilibrium condition in common case

$$RT\ln\left(\gamma_{Si}x_{Si}\right)+\mu_{Si}^{(l)}+RT\ln\left(\gamma_{C}x_{C}\right)+\mu_{C}^{(l)}=\mu_{SiC}^{(s)}, \tag{2}$$

where γ_i, x_i and $\mu_i^{(l,s)}$ are the activity coefficient, the equilibrium mole fraction and the standard Gibbs' energy of i-th component, respectively; R is the gas constant in J·kmole^{-1}·K^{-1}, T is the temperature in Kelvin. To find the activity coefficients, the thermodynamics of non-ideal solutions [16] considers the total Gibbs' energy describing the state of a system as a whole:

$$G=\sum_{i=1}^{N_c}x_i\left[RT\ln\left(\gamma_i x_i\right)+\mu_i^{(l)}\right], \tag{3}$$

where N_c is the total number of components including the carbon. Then the deviation from ideal solution, the excess Gibbs' energy ΔG^{ex}, can be extracted from Eq. (3) as

$$\Delta G^{ex}=\sum_{i=1}^{N_c}x_i RT\ln\gamma_i. \tag{4}$$

Eq. (4) gives the relation of activity coefficients, γ_i, and ΔG^{ex}. Normally, the latter is approximated as

$$\Delta G^{ex}=\sum_{i=1}^{N_C-1}\sum_{j=i+1}^{N_C}\Delta G_{i-j}^{ex}, \tag{5}$$

where ΔG_{i-j}^{ex} is the excess Gibbs' energy of $(i-j)$-system containing the parameters of interaction between components i and j. Their most reliable values resulted from treating many measurements are found in available literature [17–32] and collected in Table 2. Using them, the activity coefficients γ_i as functions of mole fractions x_i are expressed from Eq. (4) added by the Gibbs'–Duhem relations [16]. Then common formulae are derived for arbitrary composition

$$\begin{cases} i=1,\ldots,N_c-1:\ RT\ln\gamma_i=\Delta G^{ex}+\sum_{j=1}^{N_c-1}\left(\delta_{ij}-x_j\right)\dfrac{\partial\Delta G^{ex}}{\partial x_j},\ \delta_{ij}=\begin{cases}1, & i=j\\ 0, & i\neq j\end{cases}, \\ RT\ln\gamma_{N_c}=\Delta G^{ex}-\sum_{j=1}^{N_c-1}x_j\dfrac{\partial\Delta G^{ex}}{\partial x_j},\ x_{N_c}=1-\sum_{j=1}^{N_c-1}x_j. \end{cases} \tag{6}$$

Last equations in (6) follow from taking into account the fact that there are only (N_c-1) independent components in N_c-system. Emphasize that ΔG^{ex} via the parameters listed in Table 2 depends on all binary interactions between solution components including a co-solvent (see Eq. (6)) that influences the carbon solubility through activity coefficients in Eq. (2) which represents the equilibrium condition of the reaction (1). Expressions of γ_i are substituted in Eq. (2) where the standard Gibbs' energy of dissolved carbon $\mu_C^{(l)}$ is defined from the equilibrium condition between the pure silicon melt and the SiC crystal

$$\mu_C^{(l)}=\mu_{SiC}^{(s)}-\mu_{Si}^{(l)}-\left\{RT\ln\left[\hat{\gamma}_{Si}\left(1-\hat{x}_C\right)\right]+RT\ln\left(\hat{\gamma}_C\hat{x}_C\right)\right\}. \tag{7}$$

Here, $\hat{\gamma}_{Si}$, $\hat{\gamma}_C$, and $\hat{x}_C$ describe the Si-C solution. A temperature dependence of the carbon solubility in the molten silicon equilibrated with the silicon carbide are presented in Ref. [33] through dimensionless mass fraction

Table 2. Binary interaction parameters of excess Gibbs energy description.

$$\Delta G_{i-j}^{ex} = x_i x_j \sum_{k=0}^{3} \left({}^{k}a_{i-j} + {}^{k}b_{i-j} T \right) \left(x_i - x_j \right)^k, \ \text{J·mole}^{-1}$$

i–j	${}^{0}a_{i-j}$; ${}^{0}b_{i-j}$	${}^{1}a_{i-j}$; ${}^{1}b_{i-j}$	${}^{2}a_{i-j}$; ${}^{2}b_{i-j}$	${}^{3}a_{i-j}$; ${}^{3}b_{i-j}$	Refs.
Cr–Si	–119216.57; 16.11445	–47614.70; 12.17363	0.00; 0.00	0.00; 0.00	[17]
Fe–Si	–151127.73; 29.125	–33882.38; 2.5015	33954.71; 11.2555	21289.56; 0.865	[17]
Si–Ti	–255852.17; 21.874	25025.35; –2.0023	83940.65; –6.7152	0.00; 0.00	[17]
Co–Si	–183483.8; 34.80023	–3219.5; –15.28341	34241.7; 0.00	15579.7; 0.00	[18]
Ni–Si	–208402.55; 27.13099	–121913.40; 18.80198	0.00; 0.00	145580.2; –69.55691	[19]
Si–Y	–231878.58; 0.00	–22570.43; 3.00	75072.9; –26.56	0.00; 0.00	[20]
Sc–Si	–233581; –22.8	–25537; 0.00	71642; 0.00	0.00; 0.00	[21]
Al–Si	–11340.1; –1.23394	–3530.93; 1.35993	2265.39; 0.00	0.00; 0.00	[22]
La–Si	–220000; 20.0	21500; 0.00	11000; 0.00	0.00; 0.00	[23]
Ce–Si	–276530; 22.98	24173; 10.59	64797; 0.00	–20314.7; 0.00	[24]
Pr–Si	–290000; 30	18000; 0.00	65000; 0.00	0.00; 0.00	[23]
C–Si	8700; 0.00	0.00; 0.00	0.00; 0.00	0.00; 0.00	[17]
C–Cr	–127957; –7.6695	79574; 0.00	86315; 0.00	0.00; 0.00	[17]
C–Fe	–124320; 28.5	19300; 0.00	49260; –19.0	0.00; 0.00	[17]
C–Ti	–141051; –39.5	0.00; 0.00	0.00; 0.00	0.00; 0.00	[17]
C–Co	–107940.6; 24.956	–9805.5; 0.00	0.00; 0.00	0.00; 0.00	[25]
C–Ni	–111479; 35.2685	0.00; 0.00	0.00; 0.00	0.00; 0.00	[26]
C–Y	–264500; –13.0	66000; 22.0	0.00; 0.00	0.00; 0.00	[27]
Al–C	40861.02; –33.21138	0.00; 0.00	0.00; 0.00	0.00; 0.00	[28]
C–La	–259436.3; 30.0	–159860; 0.00	–44046.6; 0.00	0.00; 0.00	[29]
C–Ce	–268285.3; 22.2	–139372.9; 0.00	–24515.3; 0.00	0.00; 0.00	[24]
C–Pr	–206169.6; –29.9	–127621.8; 0.00	–26606.5; 0.00	0.00; 0.00	[29]
C–Nd	–268285.3; 22.227	132872.9; 0.00	–24515.3; 0.00	0.00; 0.00	[30]

$$\Delta G_{Si-Nd}^{ex} = \frac{Z_{SiNd}}{2} x_{Si} x_{Nd} \left(\varepsilon_{SiNd} + \varepsilon_{SiSi} x_{Si}^2 + \varepsilon_{SiSiSiSi} x_{Si}^4 + \varepsilon_{NdNd} x_{Nd}^2 + \varepsilon_{NdNdNdNd} x_{Nd}^4 \right), \ \text{J·mole}^{-1}$$

	ε_{SiNd}	ε_{SiSi}; $\varepsilon_{SiSiSiSi}$	ε_{NdNd}; $\varepsilon_{NdNdNdNd}$	Z_{SiNd}	
Si–Nd	–57739.2 + 8.368*T*	–27196 + 10.46*T*; 2092 – 5.0208*T*	–12552 + 6.276*T*; 3138	6	[31]

$$\Delta G_{Sc-C}^{ex} = x_{Sc} x_C \left(L_{Sc} x_{Sc} + L_C x_C + L_{ScC} x_{Sc} x_C \right), \ \text{J·mole}^{-1}$$

	L_{Sc}	L_C	L_{ScC}	
Sc–C	–92308.9 – 9.55968*T*	–213713 – 9.55968*T*	–104670	[32]

$$\hat{c}_C = 475.6 \exp\left(-\frac{28400}{T} \right). \tag{8}$$

Substituting $\mu_C^{(l)}$ in (2) for $\mu_C^{(l)}$ from (7), one obtains the final non-linear equation for calculating the carbon solubility at arbitrary temperatures and compositions limited by corresponding liquidus curves

$$RT \ln\left(\gamma_{Si} x_{Si} \right) + RT \ln\left(\gamma_C x_C \right) = RT \ln\left[\hat{\gamma}_{Si} \left(1 - \hat{x}_C \right) \right] + RT \ln\left(\hat{\gamma}_C \hat{x}_C \right). \tag{9}$$

Eq. (9) is solved relative to the carbon mole fraction x_C by iteration method with account of the mass action law applied to the chemical reaction (1). Roots of Eq. (9) give the carbon solubility as a function of temperature and composition. Note that Eq. (9) together with Eqs. (5), (6) and (8) is used in all further calculations of the carbon solubility (see Figs. 2 and 3).

The model above is verified by comparing the calculations with measurements performed for three different solutions considered in Ref. [17]: 60%Si-40%Cr, 40%Si-60%Fe and 77%Si-23%Ti. The measured carbon solubility is plotted in Fig. 2 together with its estimate when SiC is dissolved in the respective solution. As seen from the plots, all calculated dependences fit fairly well with each other and are consistent with the measurements for Si-Fe and Si-Ti systems. However, there is a remarkable discrepancy between estimates and measurements for Si-Cr solution. In this connection, the authors of Ref. [17] emphasize that in the experiment for a Si-Cr solution at

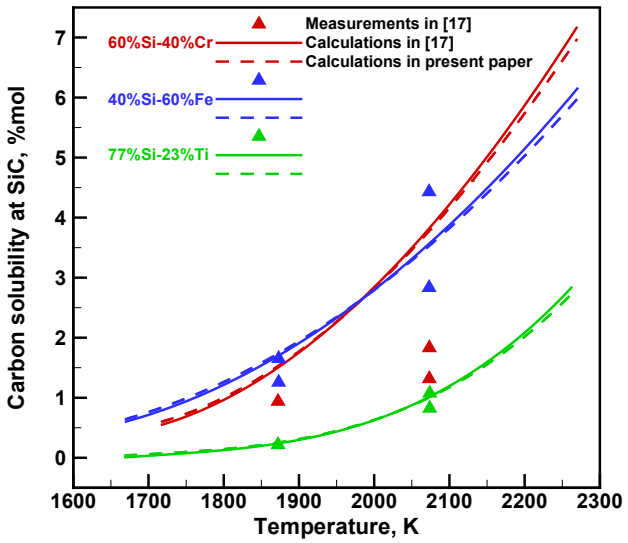

Fig. 2. Comparison of carbon solubility presented in Ref. [17] and independently calculated in the present work.

2073 K, the temperature decreased presumably within 100 K after immersing a SiC plate. With account of this fact, the calculated curves satisfactorily reproduce the measured values although the solubility seems to be overestimated. Therefore, it can be assumed that the thermodynamics of non-ideal solutions is acceptable for estimating the carbon solubility in other Si-Me systems.

2.3. Carbon solubility in binary solutions Si-Me, Me = Cr, Fe, Co, Ni, Y, Al, La, Ce, Pr, Nd and Sc

By applying the thermodynamic approach described in Section 2.2, the carbon solubility was calculated for the binary solutions saturated with SiC at temperatures and compositions varying in a wide range limited by liquidus curves. Fig. 3 shows the temperature dependence of carbon solubility at co-solvent percentages of 40, 50, 60 and 70 mol.%.

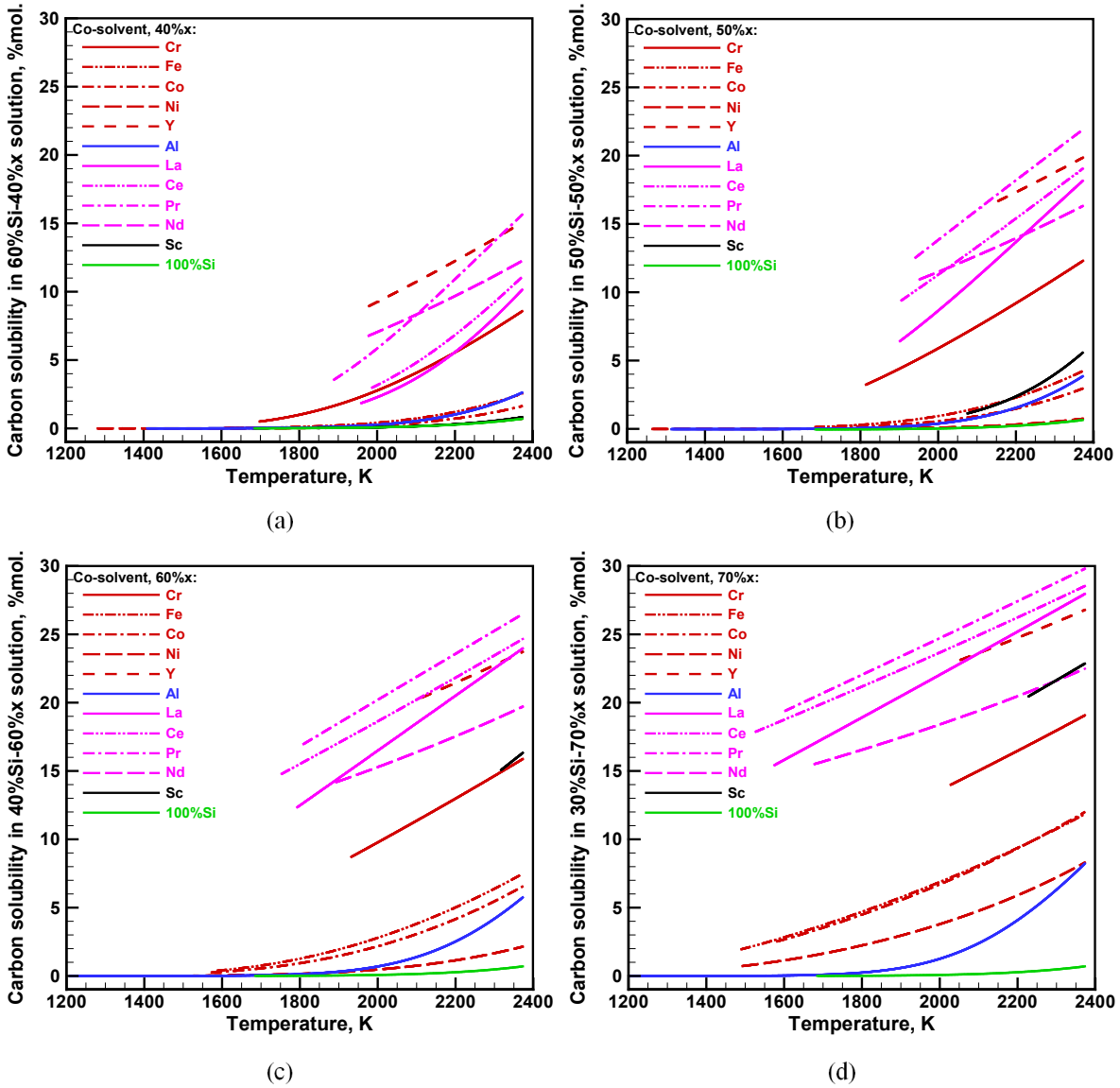

Fig. 3. Carbon solubility in binary liquid alloys equilibrated with SiC crystal vs temperature at co-solvent percentage of 40% (a), 50% (b), 60% (c) and 70% (d). Limitations of liquidus curve are accounted for (see Fig.1).

As it follows from the plots, the temperature elevation enhances the solubility, whereas its average level rises approximately twice with co-solvent percentage.

Two groups of high and low solubility can be distinguished. Silicon melt doped by Cr, La, Ce, Pr, Nd, Y and Sc is attributed to the first of them where depending on the solubility the co-solvents are approximately distributed in following sequence:

- 40%: Y (> 1979 K), Pr (> 1889 K), Nd (> 1978 K), Ce (> 1987 K), La (> 1959 K), Cr (> 1698 K);
- 50%: Pr (> 1942 K), Y (> 2155 K), Ce (> 1906 K), La (> 1902 K), Nd (> 1953 K), Cr (> 1814 K);
- 60%: Pr (> 1809 K), Ce (> 1753 K), Y (> 2113 K), La (> 1793 K), Nd (> 1893 K), Sc (> 2317 K), Cr (> 1932 K);
- 70%: Pr (> 1603 K), Ce (> 1527 K), La (> 1575 K), Y (> 2053 K), Nd (> 1678 K), Sc (> 2228 K), Cr (> 2028 K).

Here, the liquidus temperature in parentheses is shown for each binary solution in accordance with the phase diagrams (see Section 2.1). Note that the addition of Y and especially Sc results in a raised melting point. This parameter increases with Cr percentage. On the contrary, the threshold value significantly decreases with elevating the doping by lanthanides, making them most promising fluxes.

The rest of co-solvents manifests itself at high percentage. For instance, 70% of Fe, Co, Ni and Al can provide the solubility of 5–10% at temperature > 2300 K.

Particular attention should be given to a slope of solubility dependences on temperature. The larger is a slope, the steeper is a drop of solubility achievable between the C-crucible and SiC-seed in TSSG [1] and, hence, a higher growth rate. As it follows from comparing the plots in Figs. 3a, b, c and d, the variation in the slope with co-solvent percentage is clearly manifested for lanthanides. The slope decreases gradually, while a rise in the solubility moderates. Sequentially, La possesses an advantage over Pr, Pr does over Ce, Ce does over Nd. Therein, Y and Cr turn out to be less preferable. Sc has a promising steep dependence on temperature at its percentage of 60 and 70% (see Figs. 3c and d) but is extremely limited by its liquidus curve. As for other co-solvents, there is a sense in considering them at their elevated doping when providing a noticeable solubility of carbon. Among them, Al demonstrates an outstanding slope at temperature varying from 2100 to 2400 K.

2.4. Preliminary estimation of SiC growth rate

The analysis above allows one to speculate that such behavior of the slopes can lead to saturation in the growth rate with doping. To get a deeper insight into the main trends within a simplified approach, SiC growth rate is calculated between two parallel infinite plates playing a role of the C-crucible and the SiC-seed kept at different temperatures. By taking into account for the mass transport only due to diffusion, the flux of carbon J_C can be estimated as

$$J_C = -\rho D_C \frac{C_{C,seed} - C_{C,crucible}}{\Delta}, \tag{10}$$

where ρ is the solution density, D_C is the diffusion coefficient of carbon, $C_{C,seed}$ and $C_{C,crucible}$ are the equilibrium mass fractions of dissolved carbon at the seed and the crucible, respectively; Δ is the fitting parameter in meters. The solution density ρ is defined as

$$\frac{1}{\rho} = \sum_{i=1}^{N_c-1} \frac{C_{i,seed}}{\rho_i}. \tag{11}$$

To evaluate the diffusion coefficient of carbon, the Stokes-Einstein-Sutherland equation for diffusion of spherical particles through a liquid with low Reynolds number [16,34] is applied

$$D_C = \frac{RT}{N_A 6\pi r_C \eta}, \tag{12}$$

where $N_A = 6.023 \cdot 10^{26}$ kmole^{-1} is the Avogadro number, r_C is the radius of the spherical particle equal to $67 \cdot 10^{-12}$ m for the carbon atom [35], η is the viscosity coefficient of solution found according to the classic Arrhenius mixing rule for liquid mixtures [36]

$$\ln \eta = \sum_{i=1}^{N_c-1} x_i \ln \eta_i, \tag{13}$$

where η_i is the viscosity coefficient for *i*-th fluid component when flowing as a pure fluid.

Then, the SiC growth rate can be estimated as

$$V_{SiC} = \frac{M_{SiC}}{M_C} \frac{J_C}{\rho_{SiC}}, \tag{14}$$

where M_C and M_{SiC} are the molecular weights of carbon and silicon carbide, respectively; $\rho_{SiC} = 3220$ kg·m^{-3} is the SiC crystal density.

A large body of data on density and viscosity coefficient for the liquid silicon and the co-solvents investigated here were carefully analyzed in available literature. Their most reliable temperature dependences are collected in Tables 3 and 4. The sources corresponding to them are marked as first in reference list. Other sources remain as alternatives. Note that the temperature functions of density and viscosity coefficient are fitted in such a way as to agree their values (see third column of the tables) with those at melting point (see the second column) measured accurately enough in many cases. In addition, due to a lack

Table 3. Density of pure liquid substances.

$\rho_i(T) = \rho_i(T_{mi}) - C_i \cdot (T - T_{mi})$				
i	T_{mi}, K	$\rho_i(T_{mi})$, kg/m^3	C_i, kg/(m^3 · K)	References
Cr	2180	6290	0.72	[37]
Fe	1811	7034.96	0.926	[38]; [39], [37]
Co	1768	7827	0.936	[40]; [39], [37]
Ni	1728	7890	0.991	[41]; [39], [37]
Y	1796	4150	0.21	[42]; [43]
Sc	1814	2770	0.21052	[44]; [43]
Al	933	2380	0.35	[37]; [38]
La	1191	5940	0.61	[43]; [45], [46], [37]
Ce	1068	6412.492	0.831	[47]; [48], [37]
Pr	1204	6500	0.51	[46]; [43], [37]
Nd	1294	6585	0.57	[45]; [43], [48], [37]
Si	1685	2530	0.35	[37]; [49], [50], [40], [51]

Table 4. Viscosity coefficient of pure liquid substances.

$\eta_i(T) = A_i \exp\left(\frac{B_i}{RT}\right)$					
i	T_{mi}, K	η_{mi}, mPa · s	A_i, mPa · s	B_i, kJ/mole	References
Cr	2180	5.7	0.172772	63.368	[52]; [53], [54]
Fe	1811	5.8667	0.184696	52.071	[52]; [53], [38], [54]
Co	1768	5.18	0.1893374	48.64345	[52]; [53], [40], [54]
Ni	1728	4.78	0.252614	42.244	[52]; [53], [54], [55]
Y	1796	4.54	0.00287	110	[42]
Sc	1814	2.65	0.23636	36.4514	[53]
Al	933	1.38	0.2565	13.08	[53]; [38], [54]
La	1191	2.66	0.2092	25.22	[53]; [46]
Ce	1071	3.25	0.6748	13.97	[53]; [47], [54]
Pr	1204	2.85	0.9359	11.18	[53]; [46]
Nd	1294	3.19	0.351253	23.7357	[53]; [46]
Si	1685	0.58	0.1187	22.25	[52]; [49], [50], [40], [54], [53], [56]

of unambiguous information, the viscosity coefficients for liquid Cr, Fe, Co, Ni and Si are found from treating the experimental results presented in Ref. [52] while only an approximate value for liquid Sc is managed to calculate by the method suggested in Ref. [53].

The densities and viscosity coefficients calculated from formulae in Tables 3 and 4 are shown in Figs. 4 and 5 as functions of temperature varying from melting points to 2400 K. It follows from the plots that the density decreases linearly and gradually with temperature in the range of 5000–8000 kg/m^3 for Ni, Co, Fe, Cr and lanthanides, whereas Sc, Si and Al possess considerably lower density of 2000–3000 kg/m^3. In this connection, Y mediates between Sc and La.

Unlike the density, the viscosity coefficients exhibit a non-linear behavior. Cr turns out to be a most viscous co-solvent. Fe, Co and Ni follow Cr, demonstrating a steep drop in this property. Lanthanides form a separate group with a moderate dependence of viscosity on temperature where La is a least viscous co-solvent. Al and Si possess the lowest viscosity coefficients. Y is interposed between Ni and La and shows a sharpest fall with temperature varying from Y-melting point to 2400 K. Finally, Sc viscosity coefficient is higher than that of Pr and lower than that of Ni.

The properties discussed above are introduced into Eqs. (11) and (13) to calculate the carbon flux and the SiC growth rate by using Eqs. (10) and (14) at temperature and Si-Me composition varying in a wide range. Obviously, within the simplified approach accounting for only the carbon diffusion, there can be no aim and no possibility to reproduce the available experiments. Nevertheless, by

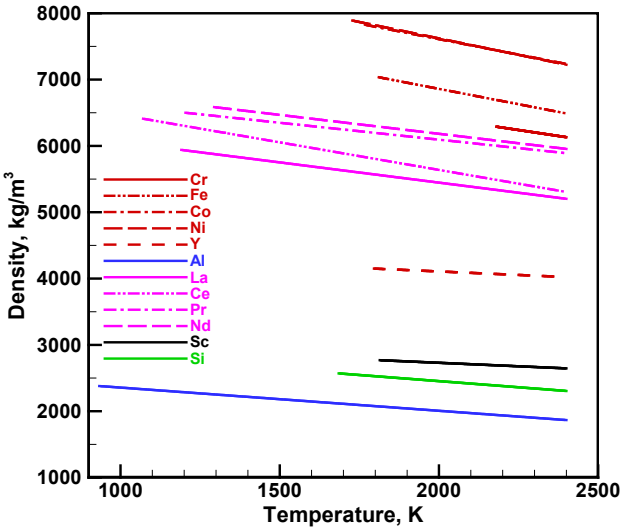

Fig. 4. Density of pure substances in Si-Me liquid alloys, where Me = Cr, Fe, Co, Ni, Y, Al, La, Ce, Pr, Nd, Sc. Limitations of liquidus curve are accounted for (see Fig. 1).

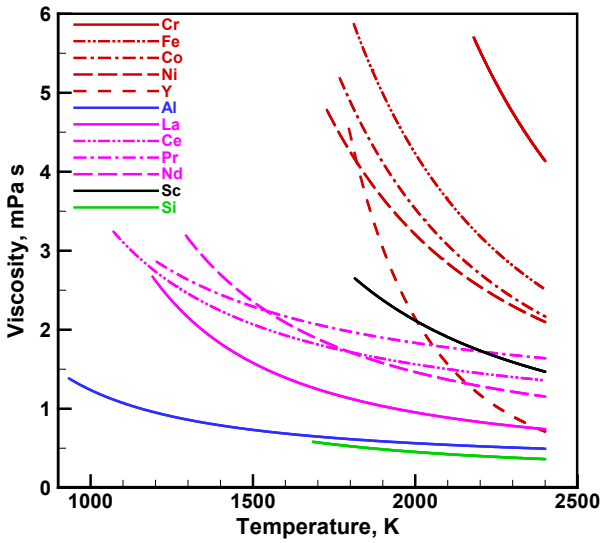

Fig. 5. Viscosity coefficient of pure substances in Si-Me liquid alloys, where Me = Cr, Fe, Co, Ni, Y, Al, La, Ce, Pr, Nd, Sc. Limitations of liquidus curve are accounted for (see Fig. 1).

comparing one with other, the effect of different co-solvents and main trends are expected to be revealed. In this connection, to agree the calculations with experiment, the undefined parameter Δ in Eq. (10) is chosen to obtain the growth rate of 200 μm/h at 2100 K and 60%Si-40%Cr as shown in Ref. [1] and is kept the same for other compositions.

Fig. 6 illustrates the estimated growth rate as a function of the co-solvent percentage at 2000, 2100, 2200 and 2300 K, while for the sake of definiteness, the temperature drop between seed (top) and crucible (bottom) is set equal to 10 K. As seen from the plots, the growth rate increases noticeably with temperature for all co-solvent except for Ni with its lowest level (long dashed red) exceeding that in pure silicon melt (solid green) only at Ni-doping of 60% and higher.

A similar behavior can be observed in the case of Sc (black solid). The growth rate here is predicted to be even lower than that in the silicon. It rises abruptly to ≈ 350 μm/h at 2300 K when Sc percentage becomes higher than 50%. Note that as it follows from Si-Sc liquidus line (see Fig. 1), 2300 K is not enough to provide Si-Sc liquid solution at Sc percentage of 60–65%.

Depending on temperature, 50–250 μm/h can be achieved at the addition of Fe (dashed dot dot red) and Co (dashed dot red) when their content becomes higher than 60%. In Si-Cr solution (solid red) the growth rate reaches a local maximum of 150–250 μm/h that slightly shifts to the left with Cr fraction. Y (dashed red) gives the growth rate considerably higher than that for the previous co-solvents. It peaks at about 35% Y and tops ≈ 200 μm/h at 2000 K and ≈ 400 μm/h at 2300 K.

As compared with others, lanthanides demonstrate highest growth rates. They are close to each other at La (solid purple) and Ce (dashed dot dot purple) and lower than that at Pr (dashed dot purple) when their percentage varies from 5 to 40%. In elevating the doping, the growth rate is saturated firstly at Pr, next at Ce and then at La. Therewith, La addition gives the greatest maximum in the growth rate while less amount of Pr and Ce is required for this. Note that the maximums shift a little bit to the left with temperature. In other words, to achieve the higher growth rate, the lower doping is needed at elevated temperatures. As for Nd, the growth rate here (long dashed purple) exceeds those of La and Ce when the doping is limited by 30–40% and is considerably lower when it is higher. Unlike other co-solvents, the local maximum is less pronounced in the dependences at Nd as well as at Cr.

Surprisingly, the growth rate increases monotonically with Al (solid blue) addition. It is remarkably lower than that of Cr, Nd, Ce, Pr, Y and La when the mole fraction of co-solvent does not exceed 40% and is predicted to achieve significant values at larger doping.

The results obtained allow one to make up some preliminary conclusions:

- SiC growth rate increases with temperature in all cases considered;
- normally, SiC growth rate begins to saturate at a certain mole fraction of co-solvent and can no longer be raised by elevating the doping, then it falls down; such behavior is consistent with some experimental data mentioned in Ref. [1] for Si-Cr solution;
- local maximum in the growth rate dependence on co-solvent percentage shifts to the left with temperature;
- on the contrary, SiC growth rate rises monotonically with Al-addition;
- a maximum possible growth rate is predicted to be provided by La-addition, and further in decreasing order - by Pr, Ce, Y, Sc, Nd, Cr, Co, Fe and Ni;

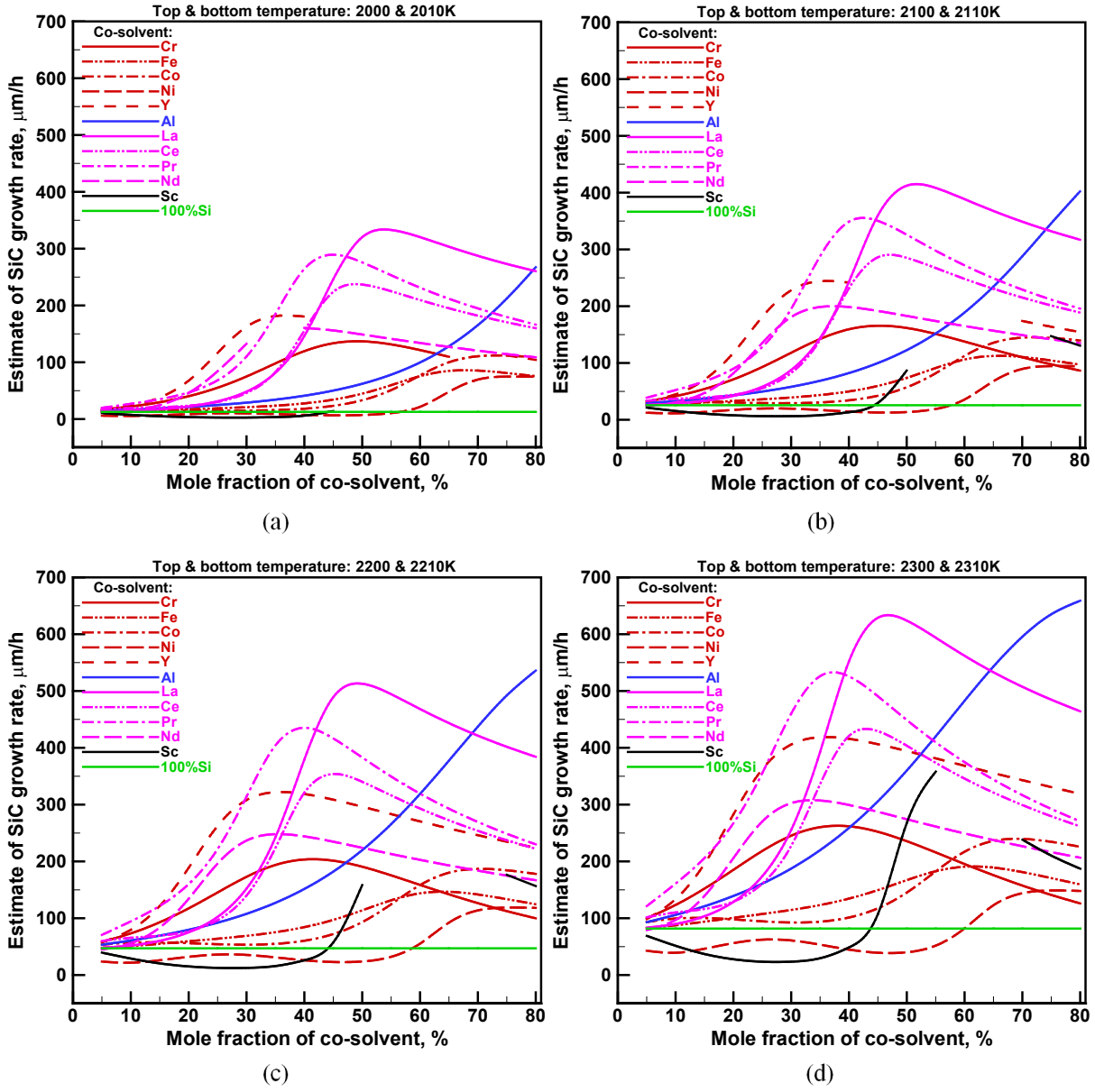

Fig. 6. Preliminary estimation of SiC growth rate in binary liquid alloys vs co-solvent percentage at seed temperature of 2000 K (a), 2100 K (b), 2200 K (c) and 2300 K (d) for temperature drop of 10 K. Gap in some dependences results from limitations of liquidus curve (see Fig. 1).

- a higher growth rate is achieved at lower content of Pr, Y, Nd and Cr (<30%) than at La and Ce.

From above comparison of growth rates, the most promising are La, Pr, Ce, Y, Nd and Cr. To support the speculation, more realistic 2D simulation should be carried out.

3. EXAMPLES OF 2D SIMULATION OF SiC TSSG

CGSim software developed by STR Group [57] is employed for 2D simulation of SiC TSSG. Modeling analog of the reactor with the seed diameter of 18 mm is considered thereto. Its schematic is shown in Fig. 7.

Thermophysical properties of solid and gas blocks (Materials) are taken from STR data base [57] while those of melt are user-defined and collected in Tables 3–7. Note that the density and viscosity coefficients of solutions are calculated as described in Section 2.4 while their heat capacity (C_p), thermal (λ) and electrical (σ) conductivity are given by following expressions from Refs. [77], [78] and [79], respectively,

$$C_p = \sum_{i=1}^{N_c-1} x_i C_{pi}, \tag{15}$$

$$\lambda = \sum_{i=1}^{N_c-1} C_i \lambda_i, \tag{16}$$

$$\sigma = \sum_{i=1}^{N_c-1} x_i \sigma_i. \tag{17}$$

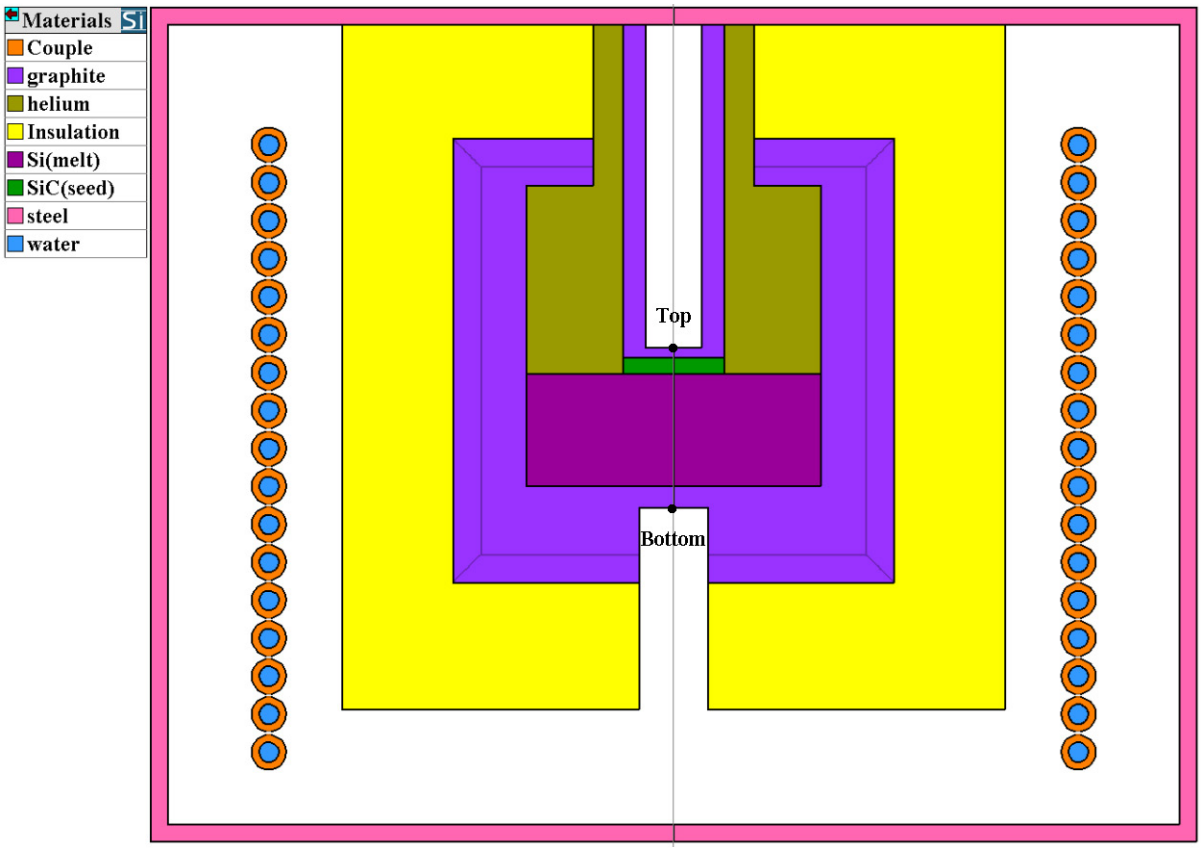

Fig. 7. Schematic of simplified set-up for simulation of SiC TSSG by CGSim software. "Top" and "Bottom" in the schematic are points where target temperatures are preset.

Table 5. Thermal conductivity of pure liquid substances.

$\lambda_i = C_{1i} + C_{2i}(T - T_{mi})$				
i	T_{mi}, K	C_{1i}, W/m/K	C_{2i}, W/m/K^2	Refs.
Cr	2180	46	0.0	[58]
Fe	1811	36.349	0.0096207	[59]
Co	1768	29.49359	0.08781	[60]
Ni	1728	54.182	0.02097	[59]
Y	1796	17.2	0.0	[61]
Sc	1814	15.8	0.0	[62]
Al	933	98	0.0	[58]
La	1191	13	0.0	[63]
Ce	1068	20.496667	0.0126614	[64]
Pr	1204	25.082333	0.0111794	[65]
Nd	1294	21.719799	0.0117000	[66]
Si	1685	66.5	0.0	[57]

Here C_{pi}, λ_i and σ_i are the heat capacity, thermal and electrical conductivity of i-th pure component in solution, respectively.

By tuning the power of inductive heater, the coupled computation of heat and mass transport are carried out in such a way as to provide the target temperatures at points marked by "Top" and "Bottom" in Fig. 7.

Table 6. Electrical resistivity of pure substances.

i	T_{mi}, K	R_i, μΩ·cm	Refs.
Cr	2180	126	[67]
Fe	1811	9.7; 138	[68]; [67]
Co	1768	6.0; 115	[69]; [67]
Ni	1728	63 + 0.0127T; 83	[37]; [67]
Y	1796	57	[70]
Sc	1814	55	[71]
Al	933	24.2, 10.7 + 0.0145T; 24.8	[37]; [58]
La	1191	138 + 0.065 (T – 1193);	[72]
		135 + (0.0170 + 1.48·10^{-6}T)×	
		(T – 1187)	[73]
Ce	1068	127 + (0.0176 + 1.7·10^{-6}T)×	[73]
		(T – 1070)	
Pr	1204	70;	[74]
		139 + (0.0186 + 1.93·10^{-6}T)×	
		(T – 1207)	[73]
Nd	1294	64;	[75]
		154 + (0.0144 + 1.13·10^{-6}T)×	
		(T – 1292)	[73]
Si	1685	0.113T – 109	[57]
		0.113T – 113	[37]

Table 7. Molecular weight and heat capacity of pure liquid substances (taken from Ref. [76]).

i	M_i, kg/kmole	C_{pi}, J/mole/K
Cr	52	39.33
Fe	56	46.024
Co	59	40.501
Ni	59	43.095
Y	89	43.095
Sc	45	44.225
Al	27	31.748
La	139	34.309
Ce	140	37.698
Pr	141	42.970
Nd	144	48.785
Si	28	27.196

As it follows from some experimental observations [80], SiC layer can cover the crucible wall due to the reaction between liquid silicon and graphite. Consequently, carbon goes from the crucible wall and diffuses through SiC layer. This layer is dissolved, providing carbon spreading into the solution. The thickness of SiC layer is supposed to remain constant after the initial stage of growth process. Therefore, the expression of the dissolution rate of SiC layer is accepted the same as that of crystal formation. Then, the same boundary conditions can be set at both graphite wall and silicon carbide seed with different kinetic constants. More detailed description can be found in CGSim manual [57].

The chemical model above is tuned by fitting the probability of carbon and silicon sticking at the seed and the graphite crucible to agree the computations with the experimental dependence of growth rate on the temperature drop between the top and the bottom [81]. The obtained results are illustrated in Fig. 8. Accounting for the lack of detailed information on the reactor design and the process conditions used by the authors of [81], the computations are reasonably consistent with the experiment. To collate the influence of various co-solvents, the same probability of sticking is set in all further computations.

As an example, two typical distributions of temperature (left) and carbon mass fraction (right) in silicon melt doped by 40% Cr and 40% La are demonstrated in Fig. 9 at top and bottom temperature of 2300 K and 2310 K, respectively. To illustrate the pattern of melt flow, the velocity vectors are plotted in the left part of the figure. Some difference in the distributions is due to that in properties of the considered solutions. As it can be seen, Si-La solution is heated up deeper and "hot tongue" from the crucible wall is longer than that for Si-Cr. Stagnation zones near the seed and the crucible bottom are predicted to be larger for Si-Cr solution that affects the distributions of

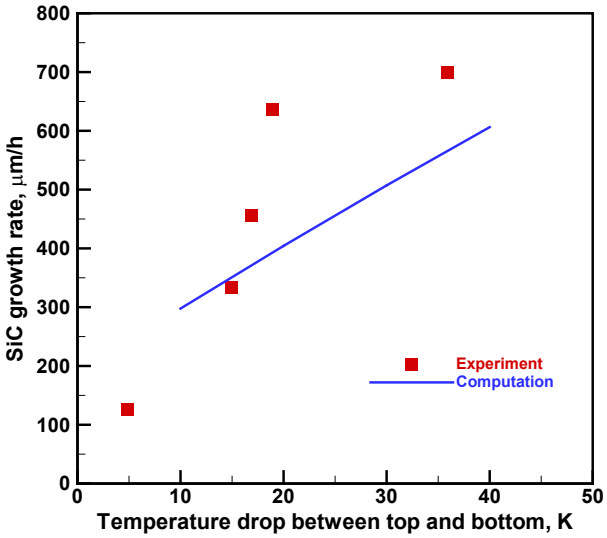

Fig. 8. Comparison of SiC growth rate given in Ref. [81] and obtained in the present work from 2D computations at bottom temperature of 2313 K and temperature drop of 10, 20, 30, 40 K between top and bottom.

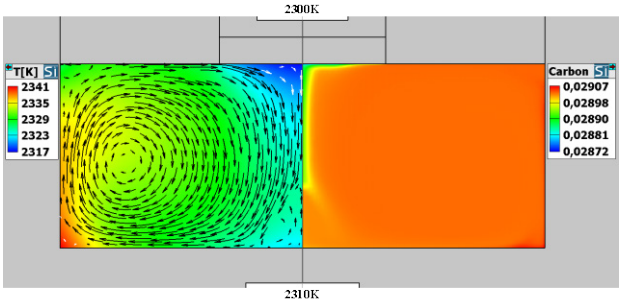

(a)

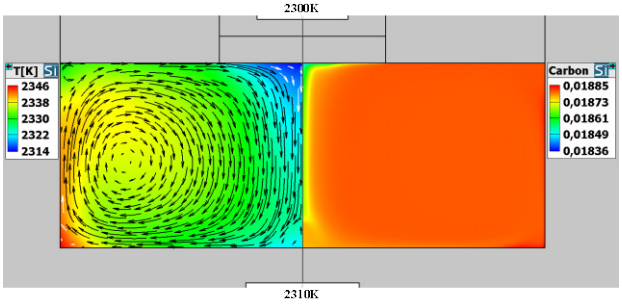

(b)

Fig. 9. Temperature and carbon distribution in silicon melt doped by 40% Cr (a) and 40% La (b). Top and bottom temperature of growth crucible is 2300 K and 2310 K, respectively. Arrows indicate the velocity vectors and illustrate the melt flow.

carbon mass fraction. Slot-like non-uniformity in carbon distribution close to the center turns out to be more extended from the seed to the bottom for Si-La solution. On the other hand, the relative variation of carbon mass fraction is lower in Si-Cr solution (1.2% vs 2.6%) in spite of the fact that its level is higher than that in Si-La solution (0.029 vs 0.018). Note that the sharp gradient of the mass fraction is located at the seed-melt interface whereas its

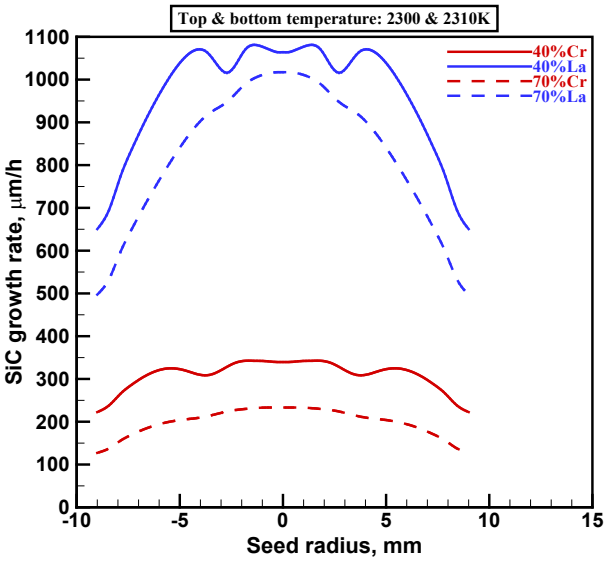

Fig. 10. Radial distribution of SiC growth rate at Cr (red) and La (blue) percentage of 40% (solid curves) and 70% (dashed curves). Top and bottom temperature is 2300 K and 2310 K, respectively.

value is close to its maximum at the crucible wall and is approximately constant over the rest of the volume. Hence one can suppose that the crystal growth occurs under kinetic limitations despite high temperatures. Support for this comes also from the dependence in Fig. 8.

Radial distributions of the growth rate are shown in Fig. 10 for 60%Si-40%Cr,La and 30%Si-70%Cr,La solutions at the same temperature regime. As is seen from the plot, the growth rate is significantly higher at La-doping than that for Cr. In addition, in both cases the crystal surface is expected to be rough at 40% doping while a practically convex crystal can be obtained by elevating Cr and La percentage to 70%. Note that the growth rate decreases with the doping considered. This agrees with the result presented in Section 2.4 (see Fig. 6) where the possible saturation in the growth rate is predicted.

4. SUMMARY

Sequential and comparative computational research is suggested to find out the effect of various co-solvents on SiC crystal growth rate from silicon melt. The information related is thoroughly analyzed and collected, including

- phase diagrams;
- interaction parameters in approximation of the excess Gibbs' energy;
- thermodynamic method of calculation of carbon solubility;
- thermophysical properties and heat and mass transport coefficients;
- kinetic chemistry at melt-solid surfaces.

Limitations attributed to liquidus-solidus of 11 binary solutions are shown and taken into account for further computations. Carbon solubility is calculated at temperature and composition varying in a wide range. Most promising solutions are preliminarily revealed. The growth rate is estimated within the simplified approach. 2D problem is set by using CGSim software, and first 2D computations are carried out, demonstrating the applicability of the model.

Further research is aimed at simulation and comparison of all binary solutions and analysis of results to optimize the solvent design.

ACKNOWLEDGEMENTS

The author is grateful to the STR administration in the person of R.A. Talalaev and V.V. Kalaev for opportunity to conduct the present research.

REFERENCES

[1] G.Q. Liang, H. Qian, Y.L. Su, L. Shi, Q. Li, Y. Liu, Review of solution growth techniques for 4H-SiC single crystal, *China Foundry*, 2023, vol. 20, no. 2, pp. 159–178.

[2] H.J. Scheel, *Introduction to liquid phase epitaxy*, in: P. Capper, M. Mauk (Eds.), *Liquid Phase Epitaxy of Electronic, Optical and Optoelectronic Materials*, John Wiley & Sons, 2007, pp. 1–19.

[3] X.F. Liu, G.G. Yan, L. Sang, Y.X. Niu, Y.W. Heb, Z.W. Shen, Z.X. Wen, J. Chen, W.S. Zhao, L. Wang, M. Guan, F. Zhang, G.S. Sun, Y.P. Zeng, Defect appearance on 4H-SiC homoepitaxial layers via molten KOH etching, *J. Cryst. Growth*, 2020, vol. 531, art. no. 125359.

[4] N. Komatsu, T. Mitani, T. Takahashi, K. Tomohisa, F. Kuniharu, T. Ujihara, Y. Matsumoto, K. Kurashige, H. Okumura, Growth rate and surface morphology of 4H-SiC single crystal grown under various supersaturations using Si-C solution, 2013, *Mater. Sci. Forum*, vol. 740–742, pp. 23–26.

[5] H. Okamoto, Cr-Si (Chromium-Silicon), *Journal of Phase Equilibria*, 2001, vol. 22, no. 5, p. 593.

[6] O. Kubaschewski, *IRON—Binary Phase Diagrams*, Springer Berlin, Heidelberg, 1982.

[7] L. Zhang, Y. Du, H. Xu, Z. Pan, Experimental investigation and thermodynamic description of the Co–Si system, *Calphad*, 2006, vol. 30, no. 4, pp. 470–481.

[8] E. Çadırlı, D.M. Herlach, T. Volkmann, *J. Non-Cryst. Solids*, 2010, vol. 356, no. 9–10, pp. 461–466.

[9] H. Okamoto, Si-Y (Silicon-Yttrium), *Journal of Phase Equilibria and Diffusion*, 2011, vol. 32, no. 5, pp. 475–476.

[10] S. Ikhmayies, *Phase Diagrams of Al–Si System*, in: T. Wang, X. Chen, D.P. Guillen, L. Zhang, Z. Sun, C. Wang, N. Haque, J.A. Howarter, N.R. Neelameggham, S. Ikhmayies, Y.R. Smith, L. Tafaghodi, A. Pandey (Eds.), *Energy Technology 2019. The Minerals, Metals & Materials Series*, Springer, Cham, 2019, pp. 231–237.

[11] H. Okamoto, La-Si (Lanthanum-Silicon), *Journal of Phase Equilibria and Diffusion*, 2007, vol. 28, no. 6, p. 585.

[12] H. Okamoto. Ce-Si (Cerium-Silicon), *Journal of Phase Equilibria and Diffusion*, 2011, vol. 32, no. 5, pp. 470–471.

[13] V.N. Eremenko, K.A. Meleshevich, Yu.I. Buyanov, Phazovaya diagramma sistemy Pr-Si, *Izvestiya Vuzov. Tsvetn. Metall.*, no. 3, pp. 82–87 (in Russian).
[14] A.B. Gokhale, A. Munitz, G.J. Abbaschian, The Nd-Si (Neodymium-Silicon) system, *Bulletin of Alloy Phase Diagrams*, 1989, vol. 10, pp. 246–251.
[15] H. Okamoto, Sc-Si (Scandium-Silicon), *Journal of Phase Equilibria*, 1992, vol. 13, no. 6, pp. 679–681.
[16] D. Kondepudi, I. Prigogine, *Modern thermodynamics: from heat engines to dissipative structures*, John Wiley & Sons, Ltd, 2015.
[17] T. Narumi, S. Kawanishi, T. Yoshikawa, K. Kusunoki, K. Kamei, H. Daikoku, H. Sakamoto, Thermodynamic evaluation of the C–Cr–Si, C–Ti–Si, and C–Fe–Si systems for rapid solution growth of SiC, *J. Cryst. Growth*, 2014, vol. 408, pp. 25–31.
[18] L. Zhang, Y. Du, H. Xu, Z. Pan, Experimental investigation and thermodynamic description of the Co–Si system, *Calphad*, 2006, vol. 30, no. 4, pp. 470–481.
[19] T. Tokunaga, K. Nishio, H. Ohtani, M. Hasebe, Thermodynamic assessment of the Ni–Si system by incorporating ab initio energetic calculations into the CALPHAD approach, *Calphad*, 2003, vol. 27, no. 2, pp. 161–168.
[20] Z. Zhang, M.Y. Chu, X.S. Zhao, K. Li, S.L. Shang, Z.K. Liu, J.Y. Shen, Thermodynamic modeling of the Si-Y system aided by first-principles and phonon calculations, *Calphad*, 2019, vol. 65, pp. 282–290.
[21] A. Qin, D. Liu, C. Chen, S. Liu, Y. Du, M. Wang, P. Nash, Heat contents of Sc_5Si_3 and ScSi intermetallics and thermodynamic modeling of the Sc–Si system, *Journal of Thermal Analysis and Calorimetry*, 2015, vol. 119, pp. 1315–1321.
[22] H. Feufel, T. Gödecke, H.L. Lukas, F. Sommer, Investigation of the Al-Mg-Si system by experiments and thermodynamic calculations, *J. Alloys Compd.*, 1997, vol. 247, no. 1–2, pp. 31–42.
[23] K. Xu, K. Chang, X. Zhou, L. Chen, J. Liu, Z. Deng, F. Huang, Q. Huang, Thermodynamic descriptions of the light rare-earth elements in silicon carbide ceramics, *J. Am. Ceram. Soc.*, 2020, vol. 103, no. 6, pp. 3812–3825.
[24] L. Guo, G. Wang, J. Lin, Z. Guo, Z. Zhang, H. Li, Z. Cao, W. Yuan, Enhanced carbon solubility in solvent for SiC rapid solution growth: Thermodynamic evaluation of Cr–Ce–Si–C system, *J. Rare Earths*, 2023, vol. 41, no. 8, pp. 1272–1278.
[25] A.F. Guillermet, Thermodynamic analysis of the Co–C System, *Int. J. Mater. Res.*, 1987, vol. 78, no. 10, pp. 700–709.
[26] H. Ohtani, M. Yamano, M. Hasebe, Thermodynamic analysis of the Co–Al–C and Ni–Al–C systems by incorporating ab initio energetic calculations into the CALPHAD approach, *Calphad*, 2004, vol. 28, no. 2, pp. 177–190.
[27] J. Gröbner, H.-L. Lukas, F. Aldinger, Thermodynamic calculations in the Y-A1-C system, *J. Alloys Compd.*, 1995, vol. 220, no. 1–2, pp. 8–14.
[28] S. Kawanishi, K. Matsunaga, T. Yoshikawa, K. Morita, Thermodynamics and Kinetics of Direct Synthesis of Solar Grade Silicon from Metallurgical Silicon Wafer by Liquid Phase Migration in Solid Silicon, *Mater. Trans.*, 2017, vol. 58, no. 11, pp. 1571–1580.
[29] Y. Peng, Y. Dua, L. Zhang, C. Sha, S. Liu, F. Zheng, D. Zhao, X. Yuan, L. Chen, Thermodynamic modeling of the C–RE (RE = La, Ce and Pr) systems, *Calphad*, 2011, vol. 35, no. 4, pp. 533–541.
[30] Y. Bian, K. Tang, G. Tranell, A thermodynamic assessment of the Nd–C system, *Calphad*, 2015, vol. 51, pp. 206–210.
[31] J. Kim, *Critical evaluation and thermodynamic modeling of Mg-RE-X (X = Mn, Si, Sn) systems coupled with experimental investigation*, Ph.D. Thesis, Department of Mining and Materials Engineering, McGill University, Montreal, QC, 2015.
[32] T.Ya. Velikanova, L.V. Artyukh, S.M. Ilyenko, V.M. Danilenko, Phase equilibria in the Sc-M-C ternary systems, *Calphad*, 1998, vol. 22, no. 1, pp. 69–84.
[33] K. Yanaba, M. Akasaka, M. Takeuchi, M. Watanabe, T. Narushima, Y. Iguchi, Solubility of carbon in liquid silicon equilibrated with silicon carbide, *Mater. Trans.*, *JIM*, 1997, vol. 38, no. 11, pp. 990–994.
[34] *Einstein relation (kinetic theory): Wikipedia*, URL: https://en.wikipedia.org/wiki/Einstein_relation_(kinetic_theory) (last access: 02.04.2024).
[35] E. Clementi, D.L. Raimondi, W.P. Reinhardt, Atomic Screening Constants from SCF Functions. II. Atoms with 37 to 86 Electrons, *J. Chem. Phys.*, 1967, vol. 47 no. 4, pp. 1300–1307.
[36] L. Chybowski, M. Szczepanek, K. Gawdzińska, Arrhenius Equation for Calculating Viscosity in Assessing the Dilution Level of Lubricating Oil with Diesel Oil-A Case Study of SAE 30 and SAE 40 Grade Marine Lubricating Oils, *Energies*, 2024, vol. 17, no. 2, art. no. 444.
[37] T. Iida, R.I.L. Guthrie, *The Physical Properties of Liquid Metals*, Clarendon Press, Oxford; Oxford University Press, New York, 1988.
[38] M.J. Assael, K. Kakosimos, R.M. Banish, J. Brillo, I. Egry, R. Brooks, P.N. Quested, K.C. Mills, A. Nagashima, Y. Sato, W.A. Wakeham, Reference Data for the Density and Viscosity of Liquid Aluminum and Liquid Iron, *J. Phys. Chem. Ref. Data*, 2006, vol. 35, no. 1, pp. 285–300.
[39] F. Tesfaye Firdu, P. Taskinen, *Densities of Molten and Solid Alloys of (Fe, Cu, Ni, Co) - S at Elevated Temperatures - Literature Review and Analysis*, Aalto University Publications in Materials Science and Engineering, Espoo, 2010, pp. 1–33.
[40] M.J. Assael, I.J. Armyra, J. Brillo, S.V. Stankus, J.Wu, W.A. Wakeham, Reference Data for the Density and Viscosity of Liquid Cadmium, Cobalt, Gallium, Indium, Mercury, Silicon, Thallium, and Zinc, *J. Phys. Chem. Ref. Data*, 2012, vol. 41, no. 3, art. no. 033101.
[41] J.J. Valencia, P.N. Quested, *Thermophysical Properties*, in: S. Viswanathan, D. Apelian, R.J. Donahue, B. DasGupta, M. Gywn, J.L. Jorstad, R.W. Monroe, M. Sahoo, T.E. Prucha, D. Twarog (Eds.), *ASM Handbook, Volume 15, Casting*, ASM International, 2010, pp. 468–481.
[42] P.-F. Paradis, T. Ishikawa, N. Koike, Thermophysical Properties of Molten Yttrium Measured by Non-contact Techniques, *Microgravity Sci. Technol.*, 2009, vol. 21, pp. 113–118.
[43] V.I. Kononenko, A.L. Sukhman, S.L. Gruverman, V.V. Torokin, Density and Surface Tension of Liquid Rare Earth Metals, Scandium, and Yttrium, *Phys. Stat. Sol. (a)*, 1984, vol. 84, no. 2, pp. 423–432.
[44] C. Koyama, Y. Watanabe, Y. Nakata, T. Ishikawa, Density Measurement of Molten Scandium by an Electrostatic Levitator, *Int. J. Microgravity Sci. Appl.*, 2020, vol. 37, no. 3, art. no. 370303.
[45] P.-F. Paradis, T. Ishikawa, N. Koike, Y. Watanabe, Study of Molten Lanthanum, Praseodymium, and Neodymium by Electrostatic Levitation, *J. Jap. Soc. Microgravity Appl.*, 2008, vol. 25, no. 3, pp. 407–412.
[46] T. Ishikawa, J.T. Okada, J. Li, P.-F. Paradis, Y. Watanabe, *Thermophysical Properties of Liquid and Supercooled Rare*

Earth Elements Measured by an Electrostatic Levitator, JAXA Research and Development Report, Japan Aerospace Exploration Agency, 2009, pp. 1–14.
[47] J. Li, T. Ishikawa, J.T. Okada, Y. Watanabe, J. Yu, S. Yoda, Z. Yuan, Noncontact thermophysical property measurement of liquid cerium by electrostatic levitation, *J. Mater. Res*., 2009, vol. 24, no. 7, pp. 2449–2452.
[48] W.G. Rohr, The liquid densities of cerium and neodymium metals, *Journal of the Less Common Metals*, 1966, vol. 10, no. 6, pp. 389–391.
[49] H. Daikoku, S. Kawanishi, T. Ishikawa, T. Yoshikawa, Density, surface tension, and viscosity of liquid Si–Cr alloys and influence on temperature and fluid flow during solution growth of SiC, *J. Chem. Thermodynamics*, 2021, vol. 160, art. no. 106476.
[50] K.C. Mills, L. Courtney, Thermophysical Properties of Silicon, *ISIJ Int.*, 2000, vol. 40, pp. S130–S138.
[51] R.K. Endo, Y. Fujihara, M. Susa, Calculation of the density and heat capacity of silicon by molecular dynamics simulation, *High Temp. High Press.*, 2003, vol. 35–36, no. 5, pp. 505–511.
[52] Y. Sato, Representation of the Viscosity of Molten Alloy as a Function of the Composition and Temperature, *Jap. J. Appl. Phys.*, 2011, vol. 50, no. 11S, art. no. 11RD01.
[53] T. Iida, R. Guthrie, M. Isac, N. Tripathi, Accurate Predictions for the Viscosities of Several Liquid Transition Metals, Plus Barium and Strontium, *Metall. Mater. Trans. B*, 2006, vol. 37B, pp. 403–412.
[54] L. Battezzati, A.L. Greer, The viscosity of liquid metals and alloys, *Acta Metall.*, 1989, vol. 37, no. 7, pp. 1791–1802.
[55] F.J. Cherne III, P.A. Deymier, Calculation of viscosity of liquid nickel by molecular dynamics methods, *Scr. Mater.*, 1998, vol. 39, no. 11, pp. 1613–1616.
[56] Y. Sato, Y. Kameda, T. Nagasawa, T. Sakamoto, S. Moriguchi, T. Yamamura, Y. Waseda, Viscosity of molten silicon and the factors affecting measurement, *J. Cryst. Growth*, 2003, vol. 249, no. 3–4, pp. 404–415.
[57] *STR Group: official website*, URL: https://str-soft.com/ (last access: 02.04.2024).
[58] *Thermophysical properties of materials for nuclear engineering: A tutorial and collection of data*, International Atomic Energy Agency, Nuclear Power Technology Development Section, Vienna, Austria, 2008.
[59] M.J. Assael, A. Chatzimichailidis, K.D. Antoniadis, W.A. Wakeham, M.L. Huber H. Fukuyama, Reference correlations for the thermal conductivity of liquid copper, gallium, indium, iron, lead, nickel and tin, *High Temp. High Press.*, 2017, vol. 46, no. 6, pp. 391–416.
[60] M.J. Assael, K.D. Antoniadis, W.A. Wakeham, M.L. Huber, H. Fukuyama, Reference correlations for the thermal conductivity of liquid bismuth, cobalt, germanium, and silicon, *J. Phys. Chem. Ref. Data*, 2017, vol. 46, no. 3, art. no. 033101.
[61] *Yttrium properties*, URL: https://material-properties.org/yttrium-thermal-properties-melting-point-thermal-conductivity-expansion/ (last access 02.04.2024).
[62] *Scandium properties*, URL: https://material-properties.org/scandium-thermal-properties-melting-point-thermal-conductivity-expansion/ (last access: 02.04.2024).
[63] *Lanthanum properties*, URL: https://material-properties.org/lanthanum-thermal-properties-melting-point-thermal-conductivity-expansion/ (last access: 02.04.2024).
[64] I.V. Savchenko, D.A. Samoshkin, S.V. Stankus, Thermal Diffusivity Measurement of Cerium in the Temperature Range of 300–1800 K, *J. Eng. Thermophys.*, 2020, vol. 29, no. 1, pp. 42–48.
[65] D.A. Samoshkin, A.Sh. Agazhanov, S.V. Stankus, Heat transfer coefficients of praseodymium in condensed state, *J. Phys.: Conf. Ser.*, 2019, vol. 1382, art. no. 012187.
[66] D.A. Samoshkin, I.V. Savchenko, S.V. Stankus, A.Sh. Agazhanov, Thermal Diffusivity and Thermal Conductivity of Neodymium in the Temperature Range 293 to 1773 K, *J. Eng. Thermophys.*, 2018, vol. 27, no. 4, pp. 399–404.
[67] J.B. Van Zytveld, Electrical resistivity of liquid chromium, *J. Non-Cryst. Solids*, 1984, vol. 61–62, part 2, pp. 1085–1090.
[68] *Technical data for the element Iron in the Periodic Table*, URL: https://periodictable.com/Elements/026/data.html (last access: 02.04.2024).
[69] *Technical data for the element Cobalt in the Periodic Table:* URL: https://periodictable.com/Elements/027/data.html (last access: 02.04.2024).
[70] *Technical data for the element Yttrium in the Periodic Table*, URL: https://periodictable.com/Elements/039/data.html (last access: 02.04.2024).
[71] *Technical data for the element Scandium in the Periodic Table*, URL: https://periodictable.com/Elements/021/data.html (last access: 02.04.2024).
[72] G. Krieg, R.B. Genter, A.V. Grosse, Electrical conductivity of liquid lanthanum, *Inorg. Nucl. Chem. Lett.*, 1969, vol. 5, no. 10, pp. 819–823.
[73] V.G. Postovalov, E.P. Romanov, V.P. Kondrat'ev, Structural Characteristics and the Temperature Derivative of the Electrical Resistivity of Liquid Lanthanides, *Phys. Metals Metallogr.*, 2007, vol. 103, no. 3, pp. 234–245.
[74] *Technical data for the element Praseodymium in the Periodic Table*, URL: https://periodictable.com/Elements/059/data.html (last access: 02.04.2024).
[75] *Technical data for the element Neodymium in the Periodic Table*, URL: https://periodictable.com/Elements/060/data.html (last access: 02.04.2024).
[76] I. Barin, *Thermochemical Data of Pure Substances*, VCH, Weinheim, Federal Republic of Germany, 1995.
[77] M.J. Blandamer, J.C.R. Reis, *A Notebook for Topics in Thermodynamics of Solutions and Liquid Mixtures*, LibreTexts, 2024, p. 1.15.5: Heat Capacities: Isochoric: Liquid Mixtures: Ideal (last access: 02.04.2024).
[78] R.L. Rowley, G.L. White, M. Chiu, Ternary liquid mixture thermal conductivities, *Chem. Eng. Sci.*, 1988, vol. 43, no. 2, pp. 361–371.
[79] C.Y. Ho, M.W. Ackerman, K.Y. Wu, T.N. Havill, R.H. Bogaard, R.A. Matula, S.G. Oh, H.M. James, Electrical Resistivity of Ten Selected Binary Alloy Systems, *J. Phys. Chem. Ref. Data*, 1983, vol. 12, no.2, pp. 183–322.
[80] J.-Y. Yoon, M.-H. Lee, Y. Kim, W.-S. Seo, Y.-G. Shul, W.-J. Lee, S.-M. Jeong, Enhancement in the rate of the top seeded solution growth of SiC crystals via a roughening of the graphite surface, *Jap. J. Appl. Phys.*, 2017, vol. 56, no. 6, art. no. 065501.
[81] T. Mitani, N. Komatsu, T. Takahashi, T. Kato, K. Fujii, T. Ujihara, Y. Matsumoto, K. Kurashige, H. Okumura, Growth rate and surface morphology of 4H–SiC crystals grown from Si–Cr–C and Si–Cr–Al–C solutions under various temperature gradient conditions, *J. Cryst. Growth*, 2014, vol. 401, pp. 681–685.

УДК 538.91+539.374.1

Численный анализ роста карбида кремния из расплава кремния, разбавленного Cr, Fe, Co, Ni, Y, Al, La, Ce, Pr, Nd и Sc. Часть 1

А.Н. Воробьев[1,2]

[1] АО «ГРУППА СТР» – ООО «Софт-импакт», Большой Сампсониевский пр., 64 литера «Е», офис 603, Санкт-Петербург, 194044, Россия
[2] НПО «Стекло и керамика», ул. Дудко, 3, Санкт-Петербург, 192029, Россия

Аннотация. Влияние различных присадок на скорость роста кристаллического карбида кремния из растворов последовательно анализируется в рамках численного подхода. Информация, относящаяся к проблеме, найдена в имеющейся литературе и тщательно переработана. Ограничения, связанные с линией плавления-затвердевания растворов, определены из фазовых диаграмм 11 бинарных систем и учитываются в расчётах растворимости углерода при изменении температуры и состава в широких пределах. Физические свойства и коэффициенты переноса собраны для предварительной оценки и сопоставления скоростей роста. Предсказывается их насыщение и последующее падение с увеличением содержания присадок. Формулируется двухмерная задача, и демонстрируются первые двухмерные расчёты. Показывается, что добавление лантана к расплаву кремния обеспечивает существенно большую скорость роста, чем при добавлении хрома.

Ключевые слова: рост карбида кремния; расплав кремния; раствор; растворимость углерода; МРК (моделирование роста кристаллов)